Kinetic effects of thermal ions and energetic particles on discrete kinetic BAE mode generation and symmetry breaking

Z. X. Lu[1], X. Wang[1], Ph. Lauber[1], F. Zonca[2,3]

[1] Max Planck Institut für Plasmaphysik, Garching, Germany
[2] ENEA C.R. Frascati, Via Enrico Fermi 45, CP 65-00044 Frascati, Italy
[3] Institute for Fusion Theory and Simulation and Department of Physics, Zhejiang University, Hangzhou 310027, People's Republic of China

Abstract. The kinetic effects of both thermal ions and energetic particles (EPs) on global Alfvén mode generation and structure symmetry breaking are important for the understanding of resonant excitation and EP transport in tokamak plasmas. In this work, the formulation for the study of the beta induced Alfvén eigenmode (BAE) driven by EPs is derived for weakly coupled poloidal harmonics with finite Larmor radius (FLR) and finite orbit width (FOW). Agreement between the theoretical model and corresponding XHMGC simulations is demonstrated. It is shown that including FLR and FOW can lead to the global mode structure broadening. The non-perturbative effects of the energetic particles on global mode structure symmetry breaking is demonstrated. In particular, when the energetic particle drive shifts away from the mode rational surface, volume averaged parallel and radial wave numbers are generated in the plasma as a demonstration of EPs' role on mode structure symmetry breaking. The connection of the mode structure symmetry breaking with experimental observations using ECEI and with particle/momentum transport are discussed.

1. Introduction

The global mode structure (in radial and poloidal directions) in non-uniform tokamak plasmas and its interaction with energetic particles are related to the instability saturation mechanism and nonlinear behaviors of the energetic particle (EP)-wave system [1, 2]. The effects of energetic particles and thermal ions on global mode structure have been studied for reversed shear Alfvén eigenmode (RSAE) [3, 4, 5], Toroidal Alfvén eigenmode (TAE) [6, 7, 8, 9] and beta induced Alfvén eigenmode (BAE) [10, 11]. The beta induced Alfvén eigenmode have attracted numerous attention [10, 12, 13, 14], as a low frequency fluctuation that can interact with thermal ions and energetic particles; and, thus, can affect the plasma confinement. Understanding the Alfvénic mode structure properties in the presence of EPs can be helpful for the interpretation of underlying physics in the experimental mode structure observations using ECEI [15, 16, 17]. In addition, understanding the symmetry breaking properties in terms of up-down symmetry breaking and parallel wave number symmetry breaking is important for evaluating the intrinsic momentum transport in the presence of energetic particle driven instabilities. As shown in this work, the EPs induced symmetry breaking is characterized by interesting novel features with respect to the intensively studied micro drift instability case [18, 19, 20].

In this work, we focus on the BAE mode structure symmetry breaking by considering kinetic effects of thermal ions and energetic particles. The FLR and FOW effects have been theoretically studied in the framework of the general fishbone-like dispersion relation (GFLDR) [21, 22, 23]. While kinetic effects related to FLR effect–the called radiative or "tunneling" damping, have been studied for the kinetic TAE problem [24, 25] and implemented in LIGKA [9], a more systematic analysis of FLR/FOW effects have been considered in LIGKA in recent years. This work aims at providing a semi analytical and semi numerical solution of global mode structure symmetry breaking for low frequency kinetic BAE, as a complement of our previous symmetry breaking study for micro-turbulence, where many poloidal harmonics are coupled to form the global mode structure (strong coupling case) [26, 27]. With numerical integrals analytically performed for well passing particles, results of this work can serve as elements for analytical models of LIGKA, i.e., LIGKA-A. While global theory has been developed using the GFLDR [11] for high-n (toroidal mode number) BAE to demonstrate the "boomerang" shape structure due to the anti-Hermitian energetic particles response, this work provides a complementary approach when the observed mode structure from experiments and gyrokinetic simulations is dominated by a single ploidal harmonic (the weak coupling limit), which can also be useful for the study of beta induced Alfvén-acoustic eigenmode (BAAE) [16, 28, 14].

This work is organized as follows. In Section 2, the general gyrokinetic quasi-neutrality and vorticity equations are introduced and the reduction to the purely electromagnetic model with finite Larmor radius and finite orbit width effects in the long wavelength limit is demonstrated. The kinetic effects from thermal ions and energetic

particles are derived in terms of non-adiabatic response functions. In Section 3, the comparison between this theoretical model and XHMGC simulation [29, 30, 10] is shown. The effects of FLR and FOW effects on global mode structure generation and the non-perturbative effect of energetic particles on global mode structure symmetry breaking are analyzed. In Section 4, the discussion and an outlook are given.

2. Models and methods

2.1. Gyrokinetic quasi-neutrality and vorticity equations and general properties

We start from the gyrokinetic equation (GKE), vorticity equation (VE) and quasi-neutrality equation (QNE) [21, 22],

$$\left[v_{\parallel}\partial_{\parallel} - i(\omega - \omega_d)\right]_s \delta K_s = i\frac{e_s}{m_s}Qf_{0s}\left[J_0(a_s)(\delta\phi - \delta\psi) + \frac{\omega_{ds}}{\omega}J_0(a_s)\delta\psi\right] \ , \tag{1}$$

$$B\partial_{\parallel}\left[\frac{1}{B}\frac{k_{\perp}^2}{k_{\theta}^2}\partial_{\parallel}\delta\psi\right] + \frac{\omega^2}{v_A^2}\frac{k_{\perp}^2}{k_{\theta}^2}\left[(1 - \frac{\omega_{*pi}}{\omega}) - \frac{3}{4}b_{i,eff}\right]\delta\phi + \frac{\alpha}{q^2R^2}g\delta\psi$$

$$= \left\langle\sum_{s=i,f}\frac{4\pi e_s}{c^2 k_{\theta}^2}J_0(a_s)\omega\omega_{ds}\delta K_s\right\rangle - 3qg(\theta)\delta\psi\left(\frac{b_i}{2}\right)^{1/2}\frac{k_{\perp}}{k_{\theta}}\frac{\omega\omega_{ti}}{v_A^2}\left(1 - \frac{\omega_{*pi}}{\omega} - \frac{\omega_{*Ti}}{\omega}\right) \ , \tag{2}$$

$$\left(1 + \frac{1}{\tau}\right)(\delta\phi - \delta\psi) + \left(1 - \frac{\omega_{*pi}}{\omega}\right)b_i\delta\psi = \frac{T_i}{ne}\langle J_0(a_i)\delta K_i\rangle \ , \tag{3}$$

where $\delta\phi$ is the perturbed scalar potential, the perturbed field $\delta\psi$ is related to the parallel vector potential fluctuation $\delta A_{\parallel}$ by $\delta A_{\parallel} \equiv -i(c/\omega)\mathbf{b}\cdot\nabla\delta\psi$, the non-adiabatic perturbed particle distribution function δK_s is related to the perturbed particle distribution function δf_s by

$$\delta f_s = \frac{e_s}{m_s}\left[\frac{\partial f_{0,s}}{\partial\epsilon}\delta\phi - J_0(a_s)\frac{Qf_{0s}}{\omega}\delta\psi e^{iL_{ks}}\right] + \delta K_s e^{iL_{ks}} \ , \tag{4}$$

where $L_{ks} = (m_s c/e_s B)(\mathbf{k}\times\mathbf{b}\cdot\mathbf{v})$, $\omega_{d,s} = v_{d,s}k_{\theta}g$, $v_{d,s} = -m_s(v_{\parallel}^2 + v_{\perp}^2/2)/(\omega_{c,s}R)$, $\epsilon = v^2/2$, f_{0s} is the equilibrium distribution function, $Qf_{0s} = \omega\partial f_{0s}/\partial\epsilon + (1/\omega_{cs})\mathbf{k}\times\mathbf{b}\cdot\nabla f_{0s}$, $\omega_{cs} = e_s B/(m_s c)$, $b_s = k_{\perp}^2\rho_{ts}^2/2$, $\rho_{ts} = cm_s v_{ts}/(e_s B)$, $\omega_{ts} = v_{ts}/(qR)$, $v_{ts} = \sqrt{2T_s/m_s}$, $b_{i,eff} = b_i(1 - \omega_{*pi}/\omega - \omega_{*Ti}/\omega)$, $\alpha = -R_0 q^2\beta'$, $\beta = 8\pi P/B^2$, P is the total plasma pressure, $g = \cos\theta + (k_r/k_{\theta})\sin\theta$, $\omega_{ps} = \omega_{*s} + \omega_{*Ts}$, $\omega_{*s} = -\rho_{ts}v_{tf}k_{\theta}/(2L_{ns})$, $\omega_{*Ts} = -\rho_{ts}v_{tf}k_{\theta}/(2L_{Ts})$, $\tau = T_e/T_i$, $\langle\ldots\rangle$ indicates velocity space integral, the subscript $s = i, f, e$ indicates the thermal ions, energetic (fast) particles and electrons respectively and the compressional Alfvén mode is suppressed here, consistent with the parameter regime of our interest. Here, $J_0(a_s)$ accounts for finite Larmor radius effects using the standard notation for the Bessel function and $a_s = k_{\perp}\rho_s$. In order to avoid the confusion due to the choice of tokamak coordinate conventions [31], we assume a right handed coordinate system (r, θ, ϕ) and (R, Z, ϕ), where r, θ and ϕ are radial-like, poloidal-like and toroidal-like coordinates. The toroidal current and toroidal magnetic field are both in $\phi > 0$ direction and consistent with the choice of coordinate system, $\mathbf{B} = \nabla\phi\times\nabla\psi_p - \nabla\theta\times\nabla\psi_t$, where ψ_p and ψ_t are pooidal and toroidal magnetic flux functions respectively with $d\psi_p/dr > 0$ and $d\psi_t/dr > 0$. Furthermore, for simplicity,

we assume high aspect-ratio, low-pressure tokamak plasma equilibrium with concentric circular magnetic flux surfaces; and the ion mass is assumed to be the same for thermal ions and energetic particles. More general equations can be obtained by considering different mass and charge of thermal ions and alpha particles.

Using the integration along the unperturbed orbit, Eq. (1) yields the equation for the perturbed non-adiabatic distribution function,

$$J_0(a_s)\delta K_s = \frac{e_s}{m_s}\frac{Qf_{0s}}{w}J_0^2(a_s)\sum_{P,Q,m}J_P(\lambda_s)J_Q(\lambda_s)i^{S-P}e^{i(S-P)(\theta+\theta_r)+im\theta}$$

$$\times\left\{\frac{\Delta\phi_m}{R_{m-nq+S}}+\frac{\delta_a\delta\psi_m e^{i\theta}}{R_{m-nq+S+1}}+\frac{\delta_b\delta\psi_m e^{-i\theta}}{R_{m-nq+S-1}}\right\}\ ,\tag{5}$$

where a single toroidal harmonic is chosen and Fourier decomposition is performed in poloidal direction, i.e., $(\delta K,\delta\psi,\Delta\phi)=\sum_m(\delta K,\delta\psi,\Delta\phi)\exp(-in\phi+im\theta)$, $\Delta\phi=\delta\phi-\delta\psi$, $\theta_r=\arctan(k_\theta/k_r)$, $\delta_{a/b,s}=v_{d,s}k_{a/b}/\omega$, $k_{a/b}=k_\theta\mp ik_r$, $\lambda_s=-qRv_{d,s}k_\perp/v_\parallel$, the resonance factor $R_N\equiv Nv_\parallel/(qR\omega)-1$ and well passing particle approximation is adopted for the sake of simplicity while keeping the necessary physics such as FLR and FOW effects. Trapped particles can be taken into account following Ref. [32].

In order to illustrate the electrostatic and electromagnetic branches of Eqs. (1), (2) and (3), we derive the solution by considering the dominant terms in δK_s in the small λ_s and a_s limit, i.e., the $P=S=0$ terms. With Eq. (5) substituted into Eqs. (2) and (3), the following eigenvalue equations are obtained for the case of a single ion species:

$$\mathcal{L}_{A,m}\delta\psi_m e^{im\theta}\equiv B\partial_\parallel\left(\frac{k_\perp^2}{B}\partial_\parallel\delta\psi\right)+\frac{\omega^2}{v_A^2}k_\perp^2\left(1-\frac{\omega_{*pi}}{\omega}-\frac{3}{4}b_{i,eff}\right)\delta\psi+\frac{\alpha k_\theta(k_a e^{i\theta}+k_b e^{-i\theta})}{q^2R^2}\delta\psi$$

$$+\frac{2v_{ti}^2}{v_A^2R^2}\left\{k_a^2 e^{2i\theta}\bar{H}_{m+1}+k_a k_b\bar{H}_{m+1}+k_a k_b\bar{H}_{m-1}+k_b^2 e^{-2i\theta}\bar{H}_{m-1}\right\}\delta\psi_m e^{im\theta}$$

$$+3(k_a e^{i\theta}+k_b e^{-i\theta})q\delta\psi\left(\frac{b_i}{2}\right)^{1/2}k_\perp\frac{\omega\omega_{ti}}{v_A^2}\left(1-\frac{\omega_{*pi}}{\omega}-\frac{\omega_{*Ti}}{\omega}\right)$$

$$=-\frac{\omega^2}{v_A^2}\left(1-\frac{\omega_{*pi}}{\omega}-\frac{3}{4}b_{i,eff}\right)k_\perp^2\Delta\phi-\frac{2v_{ti}^2}{v_A^2R^2}\left\{\frac{k_a\omega}{v_{d,t}}\bar{N}_m e^{i\theta}+\frac{k_b\omega}{v_{d,t}}\bar{N}_m e^{-i\theta}\right\}\Delta\phi_m e^{im\theta}$$

$$\equiv\mathcal{R}_{A,m}\Delta\phi_m e^{im\theta}\tag{6}$$

$$\bar{D}_m\Delta\phi_m e^{im\theta}=-\left\{\left(1-\frac{\omega_{*pi}}{\omega}\right)b_i+\delta_{a,t}\bar{N}_{m+1}e^{i\theta}+\delta_{b,t}\bar{N}_{m-1}e^{-i\theta}\right\}\delta\psi_m e^{im\theta}\ ,\tag{7}$$

where the subscript i for ions is omitted, the non-adiabatic response functions, generally, for species s, are defined as

$$\bar{D}_{k,s}=1+\frac{1}{\tau}+\hat{D}_{k,s}\ ,\quad \hat{D}_{k,s}=\left\langle\frac{\kappa\bar{f}_{0s}}{R_{k,s}}\right\rangle\ ,$$

$$\bar{N}_{k,s}=\left\langle\frac{\kappa\bar{f}_{0s}\bar{v}_{d,s}}{R_{k,s}}\right\rangle\ ,\quad \bar{H}_{k,s}=\left\langle\frac{\kappa\bar{f}_{0s}\bar{v}_{d,s}^2}{R_{k,s}}\right\rangle\ ,\tag{8}$$

where $\kappa\bar{f}_{0s}=-v_{ts}^2/(2n_{0s})(Qf_{0s}/\omega)$ and $\bar{f}_{0s}=f_{0s}/n_{0s}$. By defining $\zeta_{k,s}=\Omega_{(s)}/k$, $\Omega_{(s)}\equiv\omega/\omega_{ts}$, non-adiabatic functions, for the given species, can be expressed with the argument $\zeta_{k,s}$, e.g., $\bar{D}_{k,s}=\bar{D}_s(\zeta_{k,s})$. In the following, the subscript k and s are

omitted, when no ambiguity is brought in. For thermal ions ($s = i$) with Maxwellian distribution $\bar{f}_{0i} = \exp\{-\bar{v}^2\}/(\pi^{3/2}v_{ti}^3)$, we have $\kappa_i = 1 - (\omega_{*i}/\omega)\left[1 + \eta_i\left(\bar{v}^2 - 3/2\right)\right]$ and $\bar{H}_{k,i} = (1-\omega_{*i}/\omega)\bar{F}_{k,i}-\omega_{*Ti}\bar{G}_{k,i}$. $\bar{D}_{k,s}$, $\bar{N}_{k,s}$, $\bar{F}_{k,s}$ and $\bar{G}_{k,s}$ are calculated analytically and are equivalent to D, N, F and G functions in Refs. [21, 9]. It is obtained that $\hat{D}(\zeta) = \left(1 - \frac{\omega_*}{\omega}\right)\zeta Z(\zeta) - \frac{\omega_{*T}}{\omega}\zeta\left[\zeta + \left(\zeta^2 - \frac{1}{2}\right)Z(\zeta)\right]$, $\bar{N}(\zeta) = \zeta\left(1 - \frac{\omega_*}{\omega}\right)[\zeta + \left(\zeta^2 + \frac{1}{2}\right)Z(\zeta)] - \zeta\frac{\omega_{*T}}{\omega}[\zeta\left(\zeta^2 + \frac{1}{2}\right) + \left(\zeta^4 + \frac{1}{4}\right)Z(\zeta)]$, $\bar{F}(\zeta) = \zeta^2\left(\zeta^2 + \frac{3}{2}\right) + \zeta\left(\zeta^4 + \zeta^2 + \frac{1}{2}\right)Z(\zeta)$, $\bar{G}(\zeta) = \zeta^2\left(\zeta^4 + \zeta^2 + 2\right) + \zeta\left(\zeta^6 + \frac{\zeta^4}{2} + \zeta^2 + \frac{3}{4}\right)Z(\zeta)$ and $Z(\zeta) = (1/\sqrt{\pi})\int_{-\infty}^{\infty}dx e^{-x^2}/(x - \zeta)$ is the plasma dispersion function. Equations (6) and (7) describe the Alfvénic and acoustic branches and their coupling. They are similar to fluid equations, where the Alfvénic and acoustic branches are coupled by the finite magnetic curvature (κ) [14]; and the reduction to the local description of BAE/BAAE can be readily obtained [9, 33].

2.2. Vorticity equation with FLR and FOW effects in the purely electromagnetic limit

In this work, we focus on the quasi-electromagnetic mode which corresponds to the $T_e/T_i \to 0$ limit. Then, with $\delta\phi = \delta\psi$ obtained from Eq. (3), the purely electromagnetic model is obtained from Eqs. (1) and (2), which leads to the eigenvalue equation:

$$B\partial_\parallel\left[\frac{1}{B}\nabla_\perp^2\partial_\parallel\delta\psi\right] + \nabla_\perp\cdot\frac{\omega^2}{v_A^2}\left[(1 - \frac{\omega_{*pi}}{\omega}) - \frac{3}{4}b_{i,eff}\right]\nabla\delta\psi - \frac{\alpha g k_\theta^2}{q^2 R^2}\delta\psi \tag{9}$$

$$-3qg\delta\psi\left(\frac{b_i}{2}\right)^{1/2}k_\perp k_\theta\frac{\omega\omega_{ti}}{v_A^2}\left(1 - \frac{\omega_{*pi}}{\omega} - \frac{\omega_{*Ti}}{\omega}\right)$$

$$= -\sum_{s=i,f}KPC_s \equiv \sum_{s=i,f}\frac{k_\perp^2\omega_{ti}^2q^2\bar{n}_s\tau_s}{v_A^2}\delta\psi_m e^{im\theta}\times\left\{\frac{1}{2}\sum_{\sigma=\pm 1}\bar{H}_{m-nq+\sigma,s}\right.$$

$$\left.+\rho_{ti}^2 k_\perp^2\left[\frac{\tau_s^2}{8}\left(\frac{q}{\Omega_{(i)}}\right)^2\sum_{\sigma=\pm 1,\pm 2}(-)^\sigma(m - nq + \sigma)^2\bar{W}_{m-nq+\sigma} - \frac{\tau_s}{4}\sum_{\sigma=\pm 1}\bar{O}_{m-nq+\sigma}\right]\right\},$$

where $\bar{O}_{k,s}$ and $\bar{W}_{k,s}$ account for the finite Larmor radius and finite orbit width effects respectively. For thermal ions with Maxwellian distribution function,

$$\bar{O}_{k,i} = \left\langle\frac{\kappa\bar{f}_{0i}\bar{v}_{d,i}^2\bar{v}_\perp^2}{R_{k,i}}\right\rangle = \left(1 - \frac{\omega_{*i}}{\omega}\right)\bar{T}_{k,i} - \frac{\omega_{*Ti}}{\omega}\bar{U}_{k,i} \quad, \tag{10}$$

$$\bar{W}_{k,i} = \left\langle\frac{\kappa\bar{f}_{0i}\bar{v}_{d,i}^4}{R_{k,i}}\right\rangle = \left(1 - \frac{\omega_{*i}}{\omega}\right)\bar{L}_{k,i} - \frac{\omega_{*Ti}}{\omega}\bar{M}_{k,i} \quad. \tag{11}$$

The analytical form of Eqs. (10) and (11) can be obtained as $\bar{T}(\zeta) = \zeta[\zeta^3 + \frac{5}{2}\zeta + (\zeta^4 + 2\zeta^2 + \frac{3}{2})Z]$, $\bar{U}(\zeta) = \zeta[\zeta^5 + 3\zeta^3 + \frac{13}{2}\zeta + (\zeta^6 + \frac{5}{2}\zeta^4 + \frac{9}{2}\zeta^2 + \frac{15}{4})Z]$, $\bar{L}(\zeta) = \zeta[\zeta^7 + \frac{5}{2}\zeta^5 + \frac{19}{4}\zeta^3 + \frac{63}{8}\zeta + (\zeta^8 + 2\zeta^6 + 3\zeta^4 + 3\zeta^2 + \frac{3}{2})Z]$ and $\bar{M}(\zeta) = \zeta[\zeta^9 + 2\zeta^7 + \frac{11}{2}\zeta^5 + \frac{25}{2}\zeta^3 + \frac{201}{8}\zeta + (\zeta^{10} + \frac{3}{2}\zeta^8 + 4\zeta^6 + \frac{15}{2}\zeta^4 + 9\zeta^2 + \frac{21}{4})Z]$. The details of derivation are in Appendix A and the non-adiabatic functions are consistent with those derived based on scale separation [21, 22]. In the following, the non-adiabatic response functions will be derived also for energetic particles.

For energetic particles, we assume the following slowing down distribution [34],

$$F_f = C_0\delta(\Lambda - \Lambda_0)H\left(\epsilon_b - \epsilon\right)/\epsilon^{3/2} \quad, \tag{12}$$

where $C_0 = \sqrt{2(1-\Lambda_0 B)}B\beta_f/(2^5\pi^2 m_f \epsilon_b)$, $\delta(x)$ is the Dirac delta function, ϵ_b is the birth energy, the Heaviside function $H(x) = 0$ for $x < 0$ and $H(x) = 1$ for $x > 0$, and the EP beta $\beta_f = 4\pi \int dv^3 F_f mv^2/B^2$. The effective EP temperature is defined as $T_f = \int dv^3 F_f mv^2/(2n_f)$, where n_f is EPs' equilibrium density. Generally, Qf_{0f} has contribution from $\partial f_{0s}/\partial \epsilon$ and the radial gradient of $(n_{0f}, T_{0f}, \Lambda_0, \epsilon_b)$. In this work, the EP density profile satisfies $k_\theta \rho_f q \omega_{tf}/(2\omega \varepsilon_n) \gg 1$ and thus $\partial f_{0s}/\partial \epsilon$ is negligible. In addition, the radial variation of Λ_0 and ϵ_b is assumed to be much smaller than that of n_{0s} and T_{0s}. Then, with $\kappa_f \approx -(1+\eta_f)\omega_{*,f}/\omega$, the non-adiabatic response functions can be obtained,

$$\bar{H}_{k,f} = \left\langle \frac{\kappa \bar{f}_{0f} \bar{v}_{d,f}^2}{R_{k,f}} \right\rangle = -\frac{\omega_{*f}(1+\eta_f)}{\omega}\bar{F}_{k,f} \ , \tag{13}$$

$$\bar{O}_{k,f} = \left\langle \frac{\kappa \bar{f}_{0f} \bar{v}_{d,f}^2 \bar{v}_\perp^2}{R_{k,f}} \right\rangle = -\frac{\omega_{*f}(1+\eta_f)}{\omega}\bar{T}_{k,f} \ , \tag{14}$$

$$\bar{W}_{k,s} = \left\langle \frac{\kappa \bar{f}_0 \bar{v}_{d,f}^4}{R_{k,f}} \right\rangle = -\frac{\omega_{*f}(1+\eta_f)}{\omega}\bar{L}_{k,f} \ , \tag{15}$$

$$\bar{F}_{k,f} = P_2 \zeta_{k,f}^2 \left[1 + \bar{\zeta}_{k,f}^2 \ln\left(1 - 1/\bar{\zeta}_{k,f}^2\right) \right] \ , \tag{16}$$

$$\bar{T}_{k,f} = \Lambda_0 B P_2 \zeta_{k,f}^2 \bar{\epsilon}_b \left[1 + 2\bar{\zeta}_{k,f}^2 + 2\bar{\zeta}_{k,f}^4 \ln\left(1 - 1/\bar{\zeta}_{k,f}^2\right) \right] \ , \tag{17}$$

$$\bar{L}_{k,f} = P_4 \zeta_{k,f}^2 \bar{\epsilon}_b^2 \left[4/3 + 2\bar{\zeta}_{k,f}^2 + 4\bar{\zeta}_{k,f}^4 + 4\bar{\zeta}_{k,f}^6 \ln\left(1 - 1/\bar{\zeta}_{k,f}^2\right) \right] \ , \tag{18}$$

where $P_N = (1-\Lambda_0 B/2)^N/(1-\Lambda_0 B)$, $\bar{\zeta}_{k,f}^2 = \zeta_{k,f}^2/(2(1-\Lambda_0 B)\bar{\epsilon}_b)$. With the non-adiabatic response functions substituted, Eq. (9) can be solved for the quasi electromagnetic mode such as BAE; and the energetic particles can be readily taken into account.

2.3. Global and local equations for BAE studies

In the following, as a simplified case, the parameters are chosen to study the BAE global solution for uniform thermal ions driven by EPs with uniform EP temperature but non-uniform EP density in radial direction. For comparison, local solutions are also calculated using the local parameters such as density and its gradient. Non-uniform thermal ion density and temperature and non-uniform EPs temperature can be taken into account in Eq. (9) but will not be discussed in this work. For thermal ions with uniform density and temperature, in the $|\Omega_{(i)}| \gg 1$ limit, $\bar{F}_k \approx -7/4$, $\bar{T}_k \approx -13/4$, $\bar{L}_k \approx -249/16$, and thus

$$KPC_i = \frac{k_\perp^2 \omega_{ti}^2 \delta\psi_m e^{im\theta}}{v_A^2}\left\{ \Omega_{BAE0}^2 + \rho_{ti}^2 k_\perp^2 \left[\frac{747}{64}\frac{q^4}{\Omega^2} - \frac{13q^2}{8} \right] \right\} \ , \tag{19}$$

where $\Omega_{BAE0}^2 = (7/4)q^2$ and Eq. (19) is consistent with the corresponding expression obtained in GAM studies [23]. Note that, using the parameters in Table 1, the case considered in this work is well above the marginal instability, and the damping rate due to thermal ion anti-Hermitian part is much smaller than the growth rate induced by EPs. As a result, the thermal ion damping is ignored in Eq. (19) while the drive from EP is introduced by the logarithmic function as shown in Eq. (20).

For energetic particles, uniform EP temperature is assumed with constant Λ_0, ϵ_b and T_f in the whole plasma volume. Equations 13, 14 and 15 lead to

$$KPC_f = \frac{k_\perp^2 \omega_{ti}^2 \delta\psi_m e^{im\theta}}{v_A^2} \frac{\omega_{*,f}}{\omega} \left\{ \frac{q^2}{2} P_2 \sum_{\sigma=\pm 1} \zeta_\sigma^2 \left[1 + \bar\zeta_\sigma^2 \ln\left(1 - \frac{1}{\bar\zeta_\sigma^2} \right) \right] \right.$$

$$+ \rho_{tf}^2 k_\perp^2 \left[\frac{q^4}{8} \bar\epsilon_b^2 P_4 \sum_{\sigma=\pm 1, \pm 2} (-)^\sigma \left(2\bar\zeta_\sigma^2 + 4\bar\zeta_\sigma^4 + 4\bar\zeta_\sigma^6 \ln\left(1 - \frac{1}{\bar\zeta_\sigma^2} \right) \right) \right.$$

$$\left. \left. - \frac{q^2}{4} \Lambda_0 B \bar\epsilon_b P_2 \sum_{\sigma=\pm 1} \zeta_\sigma^2 \left(1 + 2\bar\zeta_\sigma^2 + 2\bar\zeta_\sigma^4 \ln\left(1 - \frac{1}{\bar\zeta_\sigma^2} \right) \right) \right] \right\} \ . \tag{20}$$

With Eqs. (19) and (20) substituted into Eq. (9), the global equation for uniform thermal ions and energetic particles with uniform temperature becomes

$$Y_4 \nabla_\perp^4 \delta\psi + B\partial_\| \left(\frac{\nabla_\perp^2 \partial_\| \delta\psi}{B} \right) + \nabla \cdot (D_0 \nabla_\perp \delta\psi) = 0 \ , \tag{21}$$

$$D_0 = \frac{\omega^2 - \omega_{BAE}^2}{v_A^2} - \frac{\omega_{ti}^2}{v_A^2} \left(\frac{\omega_{*,f}}{\omega} \right) \bar n_f \tau_f \frac{q^2 P_2}{2} \sum_{\sigma=\pm 1} \zeta_\sigma^2 \left[1 + \bar\zeta_\sigma^2 \ln\left(1 - \frac{1}{\bar\zeta_\sigma^2} \right) \right] \ , \tag{22}$$

$$Y_4 = \frac{\omega_{ti}^2}{v_A^2} \rho_i^2 \left\{ \left[\frac{3}{8}\Omega^2 + \frac{747}{64} \frac{q^4}{\Omega^2} - \frac{13q^2}{8} \right] + \bar n_f \tau_f^2 \left(\frac{\omega_{*,f}}{\omega} \right) \right.$$

$$\times \left[\frac{q^4}{8} \bar\epsilon_b^2 P_4 \sum_{\sigma=\pm 1, \pm 2} (-)^\sigma \left(2\bar\zeta_\sigma^2 + 4\bar\zeta_\sigma^4 + 4\bar\zeta_\sigma^6 \ln\left(1 - \frac{1}{\bar\zeta_\sigma^2} \right) \right) \right.$$

$$\left. \left. - \frac{q^2}{4} \Lambda_0 B \bar\epsilon_b P_2 \sum_{\sigma=\pm 1} \zeta_\sigma^2 \left(1 + 2\bar\zeta_\sigma^2 + 2\bar\zeta_\sigma^4 \ln\left(1 - \frac{1}{\bar\zeta_\sigma^2} \right) \right) \right] \right\} \ , \tag{23}$$

where $\bar n_f = n_f/n_{i0}$ and the non-Hermitian part due to EPs is taken into account in KPC_f. In large aspect ratio and weak coupling limit, Eq. (21) reduces to

$$Y_4 \frac{\partial^4}{\partial r^4} \delta\psi_m + Y_2 \frac{\partial^2}{\partial r^2} \delta\psi_m + Y_1 \frac{\partial}{\partial r} \delta\psi_m + Y_0 \delta\psi_m = 0 \ , \tag{24}$$

where $Y_2 = D_0 - k_\|^2$, $Y_1 = \partial Y_2/\partial r$, $Y_0 = -\left[Y_2(r)k_\theta^2 + k_\| \partial^2 k_\| / \partial r^2 \right]$. In deriving Eq. (24), the large aspect ratio assumption is used in the following simplification. We ignored $O(r/R)$ terms from $(\nabla v_A)/v_A$ and $\nabla n_i/n_i$ terms due to the uniform thermal ion assumption; we used $\nabla_\perp^2 \approx (1/r)\partial/\partial r(r\partial/\partial r) + (1/r^2)\partial^2/\partial\theta^2$ which is a good approximation for $r/R \ll 1$ and consistently, we ignored the variation of the metric tensor along **B**, i.e., $\partial_\| \nabla_\perp^2 \equiv \partial_\| [(\nabla_\perp^2 \delta\psi)/\delta\psi] \approx \partial_\|(k_r^2 + m^2/r^2) = 0$ (but $\nabla_\perp^2 \partial_\| \equiv i\nabla_\perp^2 k_\|$ is kept due to finite d^2q/dr^2). Higher order corrections can be obtained by taking into account $O(r/R)$ terms and even higher order corrections but will not be calculated due to the small r/R chosen in this work.

The normalized local dispersion relation for BAE is obtained in weak coupling limit,

$$\bar Y_2 = \Omega^2 - \Omega_{BAE}^2 - \frac{(nq - m)^2}{\beta_i} - \bar C_f \frac{(1 - \Lambda B/2)^2}{1 - \Lambda B} \frac{\Omega}{2}$$

$$\times \sum_{\sigma=m\pm 1} \frac{1}{(\sigma - nq)^2} \left[1 + \bar\zeta_{\sigma,f}^2 \ln\left[1 - \frac{1}{\bar\zeta_{\sigma,f}^2} \right] \right] = 0 \ , \tag{25}$$

where the frequency is normalized with $\omega_{ti} = v_{ti}/(qR)$, $\Omega_{BAE}^2 = (7/4 + \tau) q^2$, $\bar{C}_f = -\bar{n}_f \tau_{fi} k_\theta \rho_i q^3/(2\bar{e}_f \varepsilon_{nf})$ (note $|\omega_{*,f}/\omega| \gg 1$), $\bar{e}_f = e_f/e_i$, $\tau_{fi} = T_f/T_i$, $1/\varepsilon_{nf} = R/L_{nf}$. Note that, while the local solution corresponds to a small radial scale ($k_r L_{eq} \to \infty$, where L_{eq} is the equilibrium characteristic length), EPs are still dominated by the geodesic curvature response to provide the instability drive. Namely, it is assumed that the deviation of $J_0(\lambda_f)$ away from 1 is small by assuming small $k_r \rho_f$. This applies for the $n = 2$ mode considered in this work and, as shown in Section 3, this gives a reasonable estimate of growth rate for our considered low-n mode. At the mode rational surface ($nq - m = 0$), $\zeta_\pm = \pm \Omega^f = \omega/\omega_{tf}$ and

$$\bar{D}_0 = \Omega^2 - \Omega_{BAE}^2 - \bar{C}_f \frac{(1 - \Lambda B/2)^2}{1 - \Lambda B} \Omega \left\{ 1 + \frac{\Omega^2}{(1 - \Lambda_0 B)\bar{v}_b^2} \ln \left[1 - \frac{(1 - \Lambda_0 B)\bar{v}_b^2}{\Omega^2} \right] \right\} . \quad (26)$$

3. Numerical results and comparison with XHMGC

3.1. Methods and parameters

The finite difference approach, similar to that adopted in [35] for the micro instability study, is used for solving the eigenvalue problem defined by Eq. (21), in addition to the previous Ritz method using global basis functions [27]. This finite difference approach shows capability of calculating the global BAE mode structure and can be a complement to the finite element method [36]. The following implementation for differential operators are adopted, $df_i/dr \approx \mathbf{M_1} \cdot [f_{i-1}, f_i, f_{i+1}]^T$, $d^2 f_i/dr^2 \approx \mathbf{M_2} \cdot [f_{i-1}, f_i, f_{i+1}]^T$, $d^4 f_i/dr^4 \approx \mathbf{M_4} \cdot [f_{i-2}, f_{i-1}, f_i, f_{i+1}, f_{i+2}]^T$, where $\mathbf{M_1} = [-1, 0, 1]/(2h)$, $\mathbf{M_2} = [1, -2, 1]/h^2$, $\mathbf{M_4} = [1, -4, 6, -4, 1]/h^4$, the subscript '$i$' indicates the grid index in radial direction and h is the grid size. Then the eigenvalue problem, Eq. (21), is represented as $\overline{\overline{\mathbf{M}}}(\omega) \cdot \mathbf{Y} = 0$ and the eigenvalue is obtained by solving $\det(\overline{\overline{\mathbf{M}}}(\omega)) = 0$ where 'det' indicates the matrix determinant.

Similar parameters as those in [1] are adopted. The safety factor profile is

$$q(r) = q_0 + (q_a - q_0)(r/a)^2 \ , \quad (27)$$

where $q_0 = 1.9$, $q_a = 2.3$. The choice of the parabolic form of the q profile makes the study more analytically tractable. In addition, moderate to high q value at mode rational surface (MRS) leads to small BAE damping rate [21]. The value of $q = 2$ at the mode rational surface is relevant to that in ASDEX Upgrade plasma with BAE activities [37]. The low value of the magnetic shear at MRS leads to well isolated BAE without strong coupling between different poloidal harmonics so that the mode structure properties can be clearly demonstrated. The studies based on realistic experimental profiles are beyond the scope of this work. The energetic particle density profile is

$$\bar{n}_f = \bar{n}_{f0} C_{nf0} \left\{ 1 + C_{nf1} \left[\tanh \left(\frac{r_{cf} - r}{r_{wf}} \right) - 1 \right] \right\} \ , \quad (28)$$

$$\frac{d\bar{n}_f}{dr} = -\frac{\bar{n}_{f0} C_{nf0} C_{nf1}}{r_{wf}} \left[1 - \tanh^2 \left(\frac{r_{cf} - r}{r_{wf}} \right) \right] \ , \quad (29)$$

r_c/a	a/R_0	q_c	T_e/T_i	$\rho_{i,c}/a$	$v_{i,c}/v_{A,c}$	$v_{bf,c}/v_{A,c}$	$n_{f,c}/n_{i,c}$	$\Lambda_0 B$	$v_{bf,c}/v_{crit,c}$
0.5	0.1	2	0	$0.002\sqrt{2}$	$0.06\sqrt{2}$	$0.3\sqrt{2}$	$0.006/2$	0	$\sqrt{4.15}$

Table 1. Parametes for BAE (similar to those in [1]). The subscript 'c' denotes the value at the reference radius $r = r_c$. The $\sqrt{2}$ is due to the definition of $v_t = \sqrt{2T/m}$ in this work rather than the XHMGC convention ($v_t^{XHMGC} = \sqrt{T/m}$). $n_{f,c}/n_{i,c} = 0.003$ corresponds to the on-axis value $n_{f,axis}/n_{i,c} = 0.006$.

where $C_{nf0} = \{1 + C_{nf1} [\tanh (r_{cf}/r_{wf}) - 1]\}^{-1}$. In simulation we use $C_{nf1} = 0.5$, $r_{cf} = 0.5$, $r_{wf} = 0.1$. For the base case, other parameters at the reference radius are shown in Table 1.

3.2. Comparison of eigenvalues

The real frequency and growth rate calculated using the local approximation are shown in Fig. 1 and compared with XHMGC results. HMGC is an Hybrid Magnetohydrodynamic Gyrokinetic Code [29, 30] which has been extended to take into account the kinetic effect of both thermal ions and energetic particles (XHMGC) [10]. The XHMGC results and theoretical results agree with each other reasonably. It should be noticed that the theoretical model in this work has the following approximations: (1) the drive from $\partial F_{0f}/\partial \epsilon$ is ignored due to the dominance of the $\partial F_{0f}/\partial r$ term in QF_{0f} (the ratio of the latter to the former is $\sim k_\theta \rho_f q \omega_{tf}/(2\omega\varepsilon_n) \gg 1$); (2) XHMGC uses slowing down EP distribution

$$F_f = C_0\delta(\Lambda - \Lambda_0)H(\epsilon_b - \epsilon)/(\epsilon^{3/2} + \epsilon_c^{3/2}) \tag{30}$$

in simulations, while the analytical model adopts the $\epsilon_b/\epsilon_c \gg 1$ approximation, i.e., Eq. (12), with β_f (or $n_f T_f$) matched to that in HMGC; (3) the local eigenvalue is estimated at the mode rational surface; (4) the well passing particle assumption is adopted in the theoretical model while in XHMGC, particle motion is calculated according to the equation of motion [38]. By using the analytical KPC_f, we minimized the technical complication while keeping the key features due to EPs, e.g., the Hermitian and anti-Hermitian contribution from EPs.

3.3. Kinetic effects on global mode structure formation

As shown in Fig. 2 (left), the finite orbit width effect can lead to the broadening of the global mode structure. The base case with $\rho_c^* \equiv \rho_{i,c}/a = 2\sqrt{2}\times10^{-3}$ is calculated and the mode width is comparable to that from the HMGC simulation. The FLR/FOW effects on mode width is tested by varying ρ_c^* in Y_4 while keeping other variables unchanged. As ρ_c^* increases, the mode width increases and vice versa. The non-perturbative effect of EPs on BAE mode width is a reminiscent of TAE simulation results [8]. The modification of BAE structure due to EPs can affect the EPs transport in turn.

Different eigenstates are shown on the right of Fig. 2. The different eigenstates are labeled with the quantum number $L = 0, 1, 2 \ldots$. In addition to the even parity modes,

the odd parity modes are also observed. The ground state ($L = 0$) in this case has lowest real frequency and higher states have higher real frequency. These observations are consistent with the previous general understanding [10, 2, 39, 40].

3.4. Non-perturbative effects of EPs on symmetry breaking

For weak coupling case, the dominated poloidal harmonic, referred to as "central poloidal harmonic" in the following, has much larger amplitude than its neighboring ones (cf. Fig. 5 of [41]). The global mode structure of the central poloidal harmonic is shown in Fig. 3 for EP drive (dn_f/dr) with different r_{cf} values. For EP drive with r_{cf} near $r/a = 0.5$, the radial mode structure is relatively symmetric with respect to $r = r_{cf}$ (the central column). As r_{cf}/a shifts away from 0.5, the radial mode structure symmetry breaking appears and the 2D "boomerang" structure is characterized with asymmetric tails (the left and right columns). The 2D mode structures obtained from XHMGC simulation support this theoretical results while the remaining differences compared to the theoretical results are due to the simplifications as mentioned in Section 3.2.

The parallel symmetry breaking in terms of the intensity weighted parallel ($nq - m$)$|\delta\psi|^2$ wave number is shown in Fig. 4, where $\delta\psi$ is the normalized perturbation with the maximum amplitude $|\delta\psi| = 1$ at $r \sim 0.5$. Corresponding to the symmetric radial mode structure, the volume averaged ($nq - m$)$|\delta\psi|^2$, i.e., $\langle k_\| \rangle_V$, tends to vanish due to its opposite sign and similar magnitude inside and outside r_{cf}. As r_{cf} shift away from the critical value for symmetric radial structure, the symmetry breaking of ($nq - m$)$|\delta\psi|^2$ appears and a volume averaged ($nq - m$)$|\delta\psi|^2$ can be generated. Besides the parallel symmetry breaking, the radial symmetry breaking is also observed. The symmetry breaking in radial and parallel directions are intimately connected. Figure 5 shows the effect of the EP drive location on the symmetry breaking. As r_{cf} shifts away from the critical value $r_{cf,0} \sim 0.5a$, the volume averaged k_r and $k_\|$ are generated and both increase in magnitude. The change of the volume averaged k_r and $k_\|$ is due to the non-perturbative effect of EPs. As EPs drive shifts, the peak of the $|\delta\psi|$ profile shifts in the same direction and the volume averaged $k_\|$ changes due to the finite magnetic shear. As to be shown in Section 3.5, the volume averaged k_r also changes due to the non-perturbative effect of EPs on the BAE equation with the EP contribution. Note that while the theoretical results follow the trends of the simulation results, differences are also shown and can be due to the approximations used in the analytical derivation. Firstly, the slowing down distribution Eq. 12 is used in theoretical model in order to obtain the analytical non-adiabatic response function in Eqs. 13, 14 and 15. Compared with the numerical distribution used in XHMGC shown in Eq. 30, the theoretical model underestimates the FOW and FLR effects due to the enhanced particle population in low energy range and lowered particle population in high energy range. The underestimated FOW and FLR effects lead to the underestimate of the radial structures of observed variables. As shown in Fig. 4, the ($m - nq$)$|\delta\psi|^2$ profile from theoretical calculation is narrower than that from XHMGC simulation. Consequently,

the scaling of volume averaged k_r and $k_\parallel$ with respect to the radial location of the EP drive is also underestimated. Secondly, in theoretical model, Bessel function is approximated with $J_0(k_\perp \rho_s) \approx 1 - (k_\perp \rho_s)^2/4$. For EPs with birth energy, $k_\perp \rho_{f,b} \approx 0.113$, which can leads to small but finite inaccuracy. More accurate analytical model relies on more realistic fast particle distribution function and numerical calculation of non-adiabatic functions without expansion for the Bessel function, which is beyond the scope of this work.

The generation of $\langle k_\parallel \rangle_V$ can be relevant to the wave-particle resonance and parallel residual stress/Maxwell stress in general cases. The intrinsic rotation has been extensively studied in electrostatic micro-turbulence [18, 19, 20, 42, 43, 44]. The volume averaged $k_\parallel$ and k_r are indicators of the mode structure symmetry breaking and the residual stress generation. For example, the parallel residual stress $\Pi_{r\parallel} = nm_i \langle \delta v_{E\times B} \delta v_\parallel \rangle \propto \langle k_\theta k_\parallel |\delta\phi|^2 \rangle$. The residual stress can lead to the momentum redistribution and net toroidal rotation when coupled to the plasma edge. Since the volume average is weighted by the fluctuation intensity, which is radially local (i.e., characterized by a shorter scale length than equilibrium radial profiles), the volume average itself preserves a "local" nature. It should be noted that in order to estimate the momentum transport due to EP driven electromagnetic mode, the Maxwell stress should be also included, and the spectrum average of the residual stress with different poloidal harmonics, should be calculated. Further studies related to the parallel residual stress/Maxwell stress will be carried out in the future.

3.5. Analyses based on complex Gaussian solution

The non-perturbative effects of EPs on BAE mode structure symmetry breaking can be demonstrated using the complex Gaussian solution inspired from beam tracing and complex ray tracing approaches [45, 46]. For narrow EP drive (dn_f/dr) adopted in this work, the BAE equation can be written as

$$Y_4 \frac{d^4}{dr^4}\delta\psi + \frac{d}{dr}\left[Y_2 \frac{d}{dr}\delta\psi\right] - k_\theta^2 Y_2 \delta\psi = 0 \ , \tag{31}$$

$$Y_2 = Y_{2,i}(r_{c,i}) + Y_{2,i}''(r_{c,i})\frac{(r - r_{c,i})^2}{2} + Y_{2,f}(r_{c,f}) + Y_{2,f}''(r_{c,f})\frac{(r - r_{c,f})^2}{2} \tag{32}$$

where for the sake of simplicity, a constant Y_4 and zero $\partial^2 k_\parallel/\partial r^2$ are chosen (the linear approximation of $k_\parallel$ along radial direction due to the choice of the q profile and the consequent zero $\partial^2 k_\parallel/\partial r^2$ is chosen), Y_2 is decomposed to those contributed by thermal ions ($Y_{2,i}$) and EPs ($Y_{2,f}$). $Y_{2,i}$ is expanded near $r_{c,i}$ where $\partial Y_{2,i}/\partial r_{c,i} = 0$. For the case in this work, $r_{c,i}$ is very close to the mode rational surface due to the potential well related to the magnetic field line bending term ($\propto k_\parallel^2$). $r_{c,f}$ is very close to the EPs drive center (r_{cf} in Eq. (28)). For $r_{c,i} = r_{c,f}$, the solution of Eq. (31) is symmetric with respect to $r_{c,i}$, i.e., $\delta\psi(r_{c,i} + \Delta r) = \delta\psi(r_{c,i} - \Delta r)$, and the solution near $r_{c,i}$ can be formally represented by the complex Gaussian solution,

$$A(r) = exp\{-\sigma(r - r_0)^2\} \ , \tag{33}$$

where $r_0 = r_{c,i}$ for $r_{c,i} = r_{c,f}$. Note that generally, σ and r_0 can be both complex numbers. For EPs with shifted drive center, $r_{c,f} \neq r_{c,i}$, with coordinate transform, $\tilde{r} = r + Y_{2,f}''(r_{c,i} - r_{c,f})/(Y_{2,i}'' + Y_{2,f}'')$, the equation has the similar structure with the $r_{c,f} = r_{c,i}$ case and the Gaussian like solution is

$$A(r) = exp\{-\tilde{\sigma}(\tilde{r} - r_{ci})^2\} = exp\{-\tilde{\sigma}(r - \tilde{r}_{ci})^2\} \ , \tag{34}$$

where $\tilde{r}_{c,i} = r_{c,i} + Y_{2,f}''(r_{c,f} - r_{c,i})/(Y_{2,i}'' + Y_{2,f}'')$. By calculating the complex radial wave vector k_r defined by $A(r) = exp\{i \int dr k_r\}$ using XHMGC results, the complex Gaussian solution can be verified. For real value of r_0, $Re[k_r] = 0$ and $Im[k_r] = 0$ coincide at the same radial location, as shown in the central column of Fig. (6). For the complex value of r_0, at the peak amplitude radial location ($Im[k_r] = 0$), the value of $Re[k_r]$ is nonzero, as shown in the left and right columns of Fig. (6), which supports the form of the complex Gaussian solution in Eq. (34). The analysis is similar to that for ion temperature gradient mode (ITG) [27], while in this work, the anti-Hermitian part is from EPs. The 2D structures corresponding to different values of σ and r_0 are shown in Fig. (7). Different values of (σ, r_0) for the 2D mode structure with the form $exp\{-\sigma(r - r_0)^2 + im\theta\}$ are chosen as (A) $\sigma = 50, r_0 = 0.5$, (B) $\sigma = 50 - 60i, r_0 = 0.5$, (C) $\sigma = 50 - 60i, r_0 = 0.5 + 0.02i$, (D) $\sigma = 50 + 60i, r_0 = 0.5$. Figure (7A) corresponds to the mode structure with no EP contribution (real r_0 and σ), characterized with up-down symmetry. Figure (7B) corresponds to the boomerang like mode structure with EPs and $r_{c,i} = r_{c,f}$ and thus r_0 is real but σ is complex. Figure (7C) corresponds to shifted EP drive $r_{c,i} \neq r_{c,f}$ and complex r_0, σ for which the boomerang structure has asymmetric tales. In Fig. (7D), the sign of $Im[\sigma]$ is changed compared with Fig. (7B), indicating that the radial propagation direction reversal leads to the reversal of the 2D structure. This is the reminiscent of the recent BAE/BAAE simulation, which shows that the 2D mode structure orientation reversal coincides with the reversal of the radial Poynting vector [28]. While this work focuses on BAE study, the one on one correspondence of Figure (7D) with BAAE requires more comprehensive model for proper treatment of BAAE damping and low frequency dynamics and will be studied in future.

4. Summary and conclusions

The mode structure symmetry breaking of beta induced Alfvén eigenmode due to the EPs' non-perturbative effect is studied in this work based on both theoretical analysis and numerical simulation using XHMGC. The formulae for the global analysis of weakly coupled poloidal harmonics are derived with finite Larmor radius and finite orbit width effects of thermal ions and EPs in small $k_\perp \rho_i$ limit. It is shown that the FLR and FOW effects can lead to the broadening of the global mode structure. The theoretical results agree with the numerical simulation using XHMGC in terms of eigenvalue and symmetry breaking properties such as parallel and radial wave numbers. It is shown that the non-perturbative effect of energetic particles can lead to the BAE global mode structure distortion for low-n BAE mode, similar to the high-n BAE case [11]. In
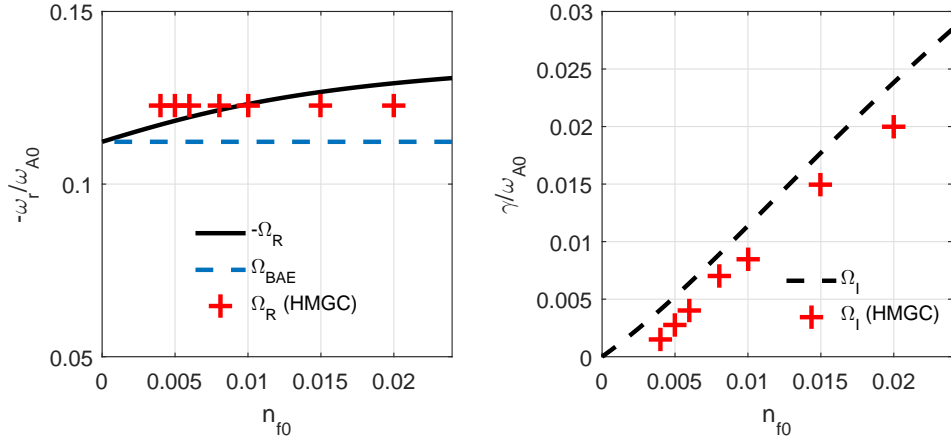
Figure 1. Comparison of local solution and global solution from XHMGC. Note that $n_f(r = r_c) = n_{f0}/2$. XHMGC includes dissipation and the result exhibits a critical n_{f0} for growth rate γ while the theoretical model ignores dissipation which is valid when the fast particle driven is not weak.
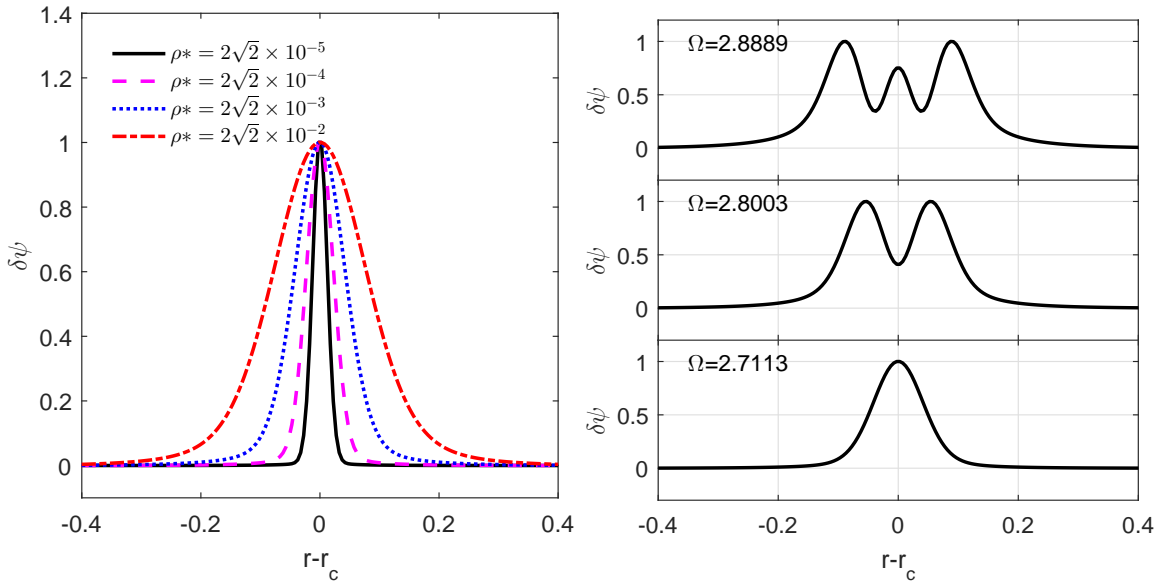

Figure 2. Left: effects of finite Larmor radius and finite orbit width on global mode width; right: different eigenstates of KBAE.

particular, in this work, the mode structure symmetry breaking in terms of parallel and radial wave numbers is observed as the EP drive shifts away from the mode rational surface. A simple complex Gaussian model solution is demonstrated to explain the non-perturbative effect of EPs on mode structure symmetry breaking.

The study of EPs' non-perturbative effects can be helpful for understanding nonlinear simulation results and underlying EP transport physics. As the EP density profile is flattened during the nonlinear stage, the drive center shifts inward or/and outward and, as observed in this work, the mode structure is modified due to the EP profile distortion. Consequently, the symmetry breaking in terms of $k_{\parallel}$ can enter the
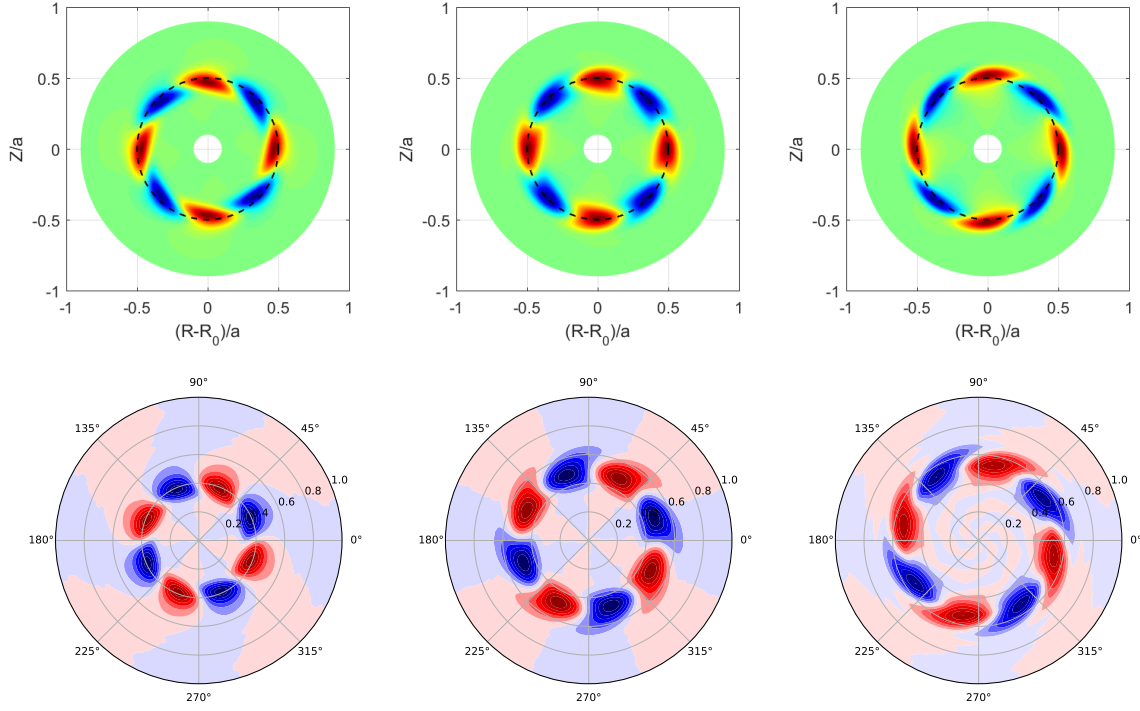
Figure 3. The 2D mode structure (first row) of BAE calculated theoretically for $r_{cf}/a = 0.42$ (left), $r_{cf}/a = 0.50$ (middle) and $r_c/a = 0.55$ (right) with EP drive in large aspect ratio limit (Eq. (24)). Second row: 2D mode structure for $r_{cf}/a = 0.42$ (left), $r_{cf}/a = 0.50$ (middle) and $r_c/a = 0.55$ calculated using XHMGC.
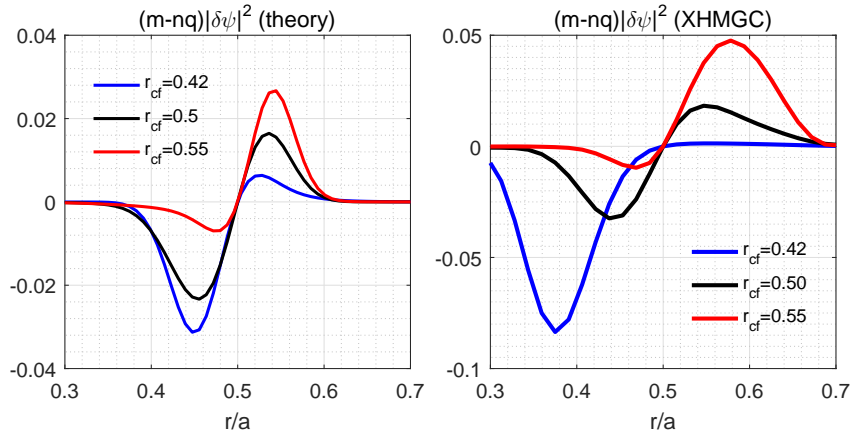

Figure 4. Radial profiles of $(m - nq)|\delta\psi|^2$ calculated theoretically (upper) and from XHMGC (lower). Only the central poloidal harmonic is kept. It is indicated that volume averaged $k_{||}|\delta\psi|^2$ is generated as EP drive center r_{cf} shifts away from BAE accumulation point.
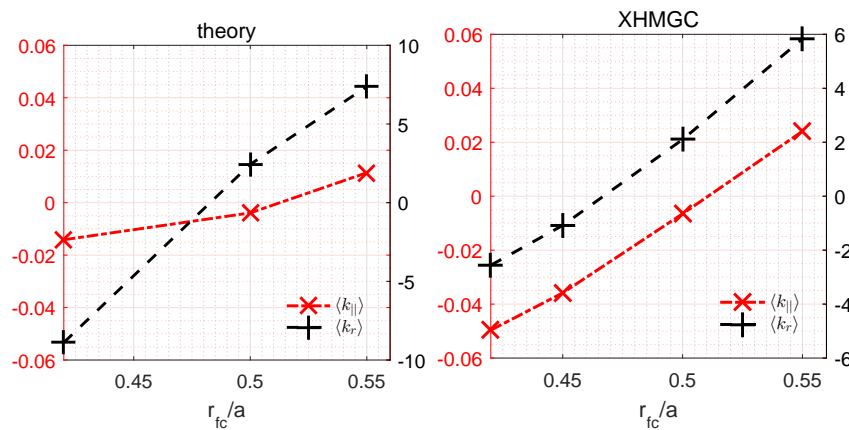
Figure 5. Volume averaged k_r and $k_{||}$ for different EP drive locations (r_{cf}).
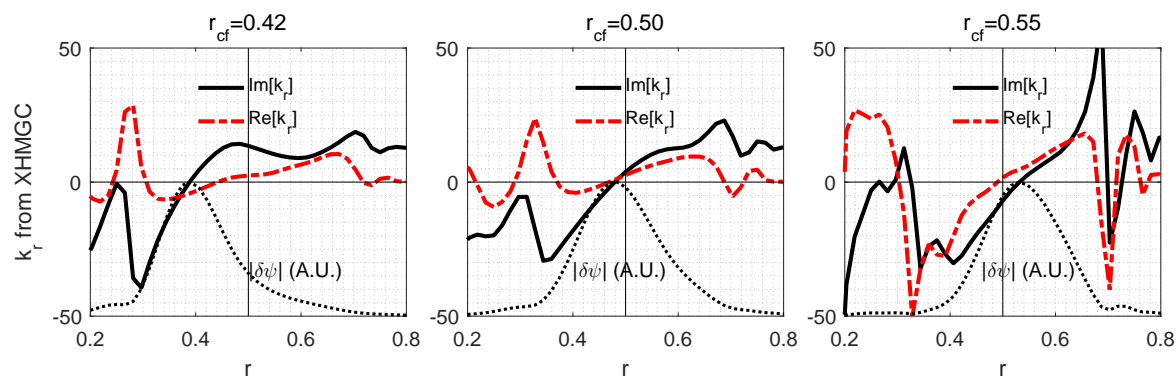

Figure 6. Profiles of $|\delta\psi(r, n = 2, m = 4)|$, $k_{r,R}$ and $k_{r,I}$ for the base case (central column) and those with shifted EP drive (left and right columns). The mismatch between the $k_{r,R} = 0$ point and the $k_{r,I} = 0$ point is observed for cases with shifted EP drive.

wave-particle resonance condition and in turn can change the EP driven instabilities. The analyses of mode structure, in particular the symmetry properties, can be helpful for identifying the interplay of EP transport and instability excitation. The relevance of BAE symmetry breaking to other problems will be analyzed in future, such as the effects of the symmetry breaking on the wave-particle interaction between EPs/thermal ions and Alfvén eigenmode and the consequent thermal ion momentum transport [42, 18] and EPs transport [47].

Appendix A. Derivation of non-adiabatic response functions

Velocity space integral of an variable A for Maxwellian distribution is given by

$$\langle A \rangle = \frac{4v_t^3}{\sqrt{\pi}} \int_0^\infty \int_0^\infty d\hat{v}_\perp d\hat{v}_{||} \hat{v}_\perp A e^{-\hat{v}^2} \ , \tag{A.1}$$

where $\hat{v} = v/v_t$. By defining $I_N \equiv \int_0^\infty dx x^N e^{-x^2}$, and noticing

$$I_0 = \frac{\sqrt{\pi}}{2} \ , \quad I_2 = \frac{\sqrt{\pi}}{4} \ , \quad I_4 = \frac{3\sqrt{\pi}}{8} \ , \quad I_6 = \frac{15\sqrt{\pi}}{16} \ , \quad I_8 = \frac{105\sqrt{\pi}}{32} \ , \quad I_{10} = \frac{945\sqrt{\pi}}{64}$$
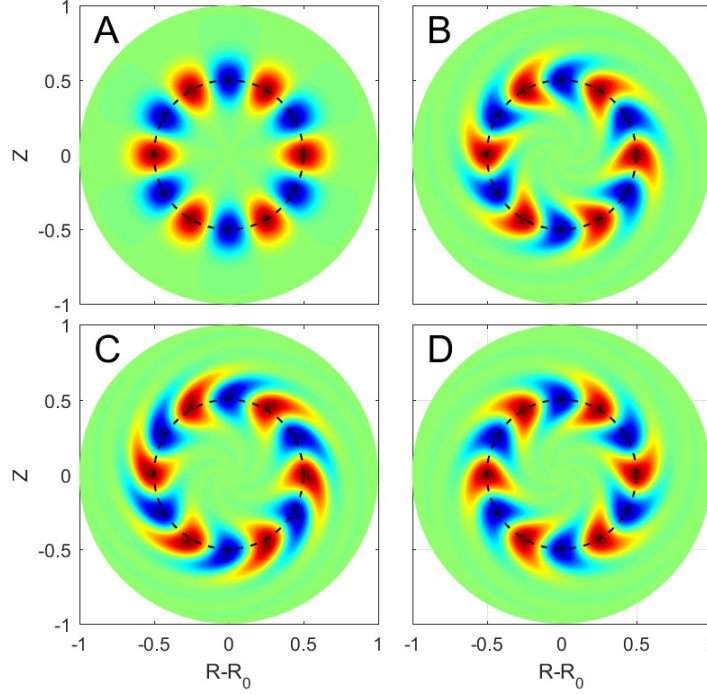
Figure 7. Different 2D structures for different values of σ and r_0 in Eq. (33). Parameters are (A) $\sigma = 50, r_0 = 0.5$, (B) $\sigma = 50 - 60i, r_0 = 0.5$, (C) $\sigma = 50 - 60i, r_0 = 0.5 + 0.02i$, (D) $\sigma = 50 + 60i, r_0 = 0.5$.

$$I_1 = \frac{1}{2} \ , \ \ I_3 = \frac{1}{2} \ , \ \ I_5 = 1 \ , \ \ I_7 = 3 \ , \ \ I_9 = 12 \ , \ \ I_{11} = 60 \ , \tag{A.2}$$

$$\langle \hat{v}_\perp^j \hat{v}_\parallel^k \rangle = \frac{4}{\sqrt{\pi}} \int_0^\infty \int_0^\infty d\hat{v}_\perp d\hat{v}_\parallel \hat{v}_\perp^j \hat{v}_\parallel^k e^{-\hat{v}^2} = \frac{4}{\sqrt{\pi}} I_{j+1} I_k \ , \tag{A.3}$$

the non-adiabatic response $\bar{W}$, $\bar{O}$ functions can be calculated readily. With $\kappa_i = 1 - \omega_{*i}/\omega \left[1 + \eta_i \left(\bar{v}^2 - 3/2 \right) \right]$ substituted, we have

$$\bar{O}_k = \left\langle \frac{\kappa \bar{f}_0 \bar{v}_d^2 \bar{v}_\perp^2}{R_k} \right\rangle = \left(1 - \frac{\omega_{*i}}{\omega} + \frac{3}{2} \frac{\omega_{*T}}{\omega} \right) \left\langle \frac{\bar{f}_0 \bar{v}_d^2 \bar{v}_\perp^2}{R_k} \right\rangle - \frac{\omega_{*T}}{\omega} \left\langle \frac{\bar{f}_0 \bar{v}_d^2 \bar{v}_\perp^2 \bar{v}^2}{R_k} \right\rangle \ , \tag{A.4}$$

$$\bar{W}_k = \left\langle \frac{\kappa \bar{f}_0 \bar{v}_d^4}{R_k} \right\rangle = \left(1 - \frac{\omega_{*i}}{\omega} + \frac{3}{2} \frac{\omega_{*T}}{\omega} \right) \left\langle \frac{\bar{f}_0 \bar{v}_d^4}{R_k} \right\rangle - \frac{\omega_{*T}}{\omega} \left\langle \frac{\bar{f}_0 \bar{v}_d^4 \bar{v}^2}{R_k} \right\rangle \ , \tag{A.5}$$

$$\left\langle \frac{\bar{f}_0 \bar{v}_d^2 \bar{v}_\perp^2}{R_k} \right\rangle \equiv \bar{T} = \zeta \left[\zeta^3 + \frac{5}{2} \zeta + \left(\zeta^4 + 2\zeta^2 + \frac{3}{2} \right) Z \right] \ , \tag{A.6}$$

$$\left\langle \frac{\bar{f}_0 \bar{v}_d^2 \bar{v}_\perp^2 \bar{v}^2}{R_k} \right\rangle = \zeta \left[\zeta^5 + \frac{9}{2} \zeta^3 + \frac{41}{4} \zeta + \left(\zeta^6 + 4\zeta^4 + \frac{15}{2} \zeta^2 + 6 \right) Z \right] \ , \tag{A.7}$$

$$\left\langle \frac{\bar{f}_0 \bar{v}_d^2 \bar{v}_\perp^2 \bar{v}^2}{R_k} \right\rangle - \frac{3}{2} \left\langle \frac{\bar{f}_0 \bar{v}_d^2 \bar{v}_\perp^2}{R_k} \right\rangle \equiv \bar{U}$$

$$= \zeta \left[\zeta^5 + 3\zeta^3 + \frac{13}{2} \zeta + \left(\zeta^6 + \frac{5}{2} \zeta^4 + \frac{9}{2} \zeta^2 + \frac{15}{4} \right) Z \right] \ , \tag{A.8}$$

$$\left\langle \frac{\bar{f}_0 \bar{v}_d^4}{R_k} \right\rangle \equiv \bar{L} = \zeta \left[\zeta^7 + \frac{5}{2} \zeta^5 + \frac{19}{4} \zeta^3 + \frac{63}{8} \zeta + \left(\zeta^8 + 2\zeta^6 + 3\zeta^4 + 3\zeta^2 + \frac{3}{2} \right) Z \right] \ ,$$

$$\text{(A.9)}$$

$$\left\langle \frac{\bar{f}_0 \bar{v}_d^4 \bar{v}^2}{R_k} \right\rangle = \zeta \left[\zeta^9 + \frac{7}{2}\zeta^7 + \frac{37}{4}\zeta^5 + \frac{157}{8}\zeta^3 + \frac{591}{16}\zeta \right.$$

$$\left. + \left(\zeta^{10} + 3\zeta^8 + 7\zeta^6 + 12\zeta^4 + \frac{27}{2}\zeta^2 + \frac{15}{2} \right) Z \right] ,$$

$$\left\langle \frac{\bar{f}_0 \bar{v}_d^4 \bar{v}^2}{R_k} \right\rangle - \frac{3}{2}\left\langle \frac{\bar{f}_0 \bar{v}_d^4}{R_k} \right\rangle \equiv \bar{M} = \zeta \left[\zeta^9 + 2\zeta^7 + \frac{11}{2}\zeta^5 + \frac{25}{2}\zeta^3 + \frac{201}{8}\zeta \right.$$

$$\left. + \left(\zeta^{10} + \frac{3}{2}\zeta^8 + 4\zeta^6 + \frac{15}{2}\zeta^4 + 9\zeta^2 + \frac{21}{4} \right) Z \right] , \qquad \text{(A.10)}$$

where $Z(\zeta) = \frac{1}{\sqrt{\pi}} \int_{-\infty}^{\infty} \frac{dx e^{-x^2}}{x-\zeta}$, $\bar{T}$, $\bar{U}$, $\bar{L}$ and $\bar{M}$ are consistent with those derived in GFLDR [22].

For slowing down EPs, the non-adiabatic response functions are obtained readily noticing,

$$\left\langle \frac{\bar{f}_f A(\epsilon)}{\bar{v}_\parallel / \zeta - 1} \right\rangle = \frac{\zeta^2}{4(1 - \Lambda_0 B)\bar{\epsilon}_b} \int_0^{\bar{\epsilon}_b} \frac{d\bar{\epsilon} A}{\bar{\epsilon}\left[\bar{\epsilon} - \frac{\zeta^2}{2(1-\Lambda_0 B)}\right]} . \qquad \text{(A.11)}$$

Acknowledgments

[1] Wang X, Briguglio S, Lauber P, Fusco V and Zonca F 2016 *Phys. Plasmas* **23** 012514
[2] Chen L and Zonca F 2016 *Rev. Modern Phys.* **88** 015008
[3] Zonca F, Briguglio S, Chen L, Dettrick S, Fogaccia G, Testa D and Vlad G 2002 *Phys. Plasmas* **9** 4939
[4] Berk H, Borba D, Breizman B, Pinches S and Sharapov S 2001 *Phys. Rev. Lett.* **87** 185002
[5] Fu G and Berk H 2006 *Phys. plasmas* **13** 052502
[6] Chen L and Zonca F 1995 *Physica Scripta* **1995** 81
[7] Zonca F and Chen L 1996 *Physics of Plasmas* **3** 323
[8] Wang Z, Lin Z, Holod I, Heidbrink W, Tobias B, Van Zeeland M and Austin M 2013 *Phys. Rev. Lett.* **111** 145003
[9] Lauber P, Brüdgam M, Curran D, Igochine V, Sassenberg K, Günter S, Maraschek M, García-Muñoz M, Hicks N and the ASDEX Upgrade Team 2009 *Plasma Phys. Controlled Fusion* **51** 124009
[10] Wang X, Zonca F and Chen L 2010 *Plasma Phys. Controlled Fusion* **52** 115005
[11] Ma R, Zonca F and Chen L 2015 *Phys. Plasmas* **22** 092501
[12] Heidbrink W W, Strait E J, Chu M S and Turnbull A D 1993 *Phys. Rev. Lett.* **71**(6) 855
[13] Zhang H S, Lin Z, Holod I *et al.* 2012 *Phys. Rev. Lett.* **109** 025001
[14] Chen L and Zonca F 2017 *Phys. Plasmas* **24** 072511

[15] Tobias B, Classen I, Domier C, Heidbrink W, Luhmann Jr N, Nazikian R, Park H, Spong D A and Van Zeeland M 2011 *Phys. Rev. Lett.* **106** 075003

[16] Heidbrink W, Van Zeeland M, Austin M, Bass E, Chen X, Grierson B, Muscatello C, Matsunaga G, McKee G, Pace D *et al.* 2012 Fast ion physics enabled by off-axis neutral beam injection *Proc. 24th Int. Conf. on Fusion Energy (San Diego, CA, 2012)*

[17] Garcia-Munoz M, Classen I, Geiger B, Heidbrink W, Van Zeeland M, Äkäslompolo S, Bilato R, Bobkov V, Brambilla M, Conway G *et al.* 2011 *Nucl. Fusion* **51** 103013

[18] Peeters A G, Angioni C, Bortolon A, Camenen Y, Casson F J, Duval B, Fiederspiel L, Hornsby W A, Idomura Y, Hein T *et al.* 2011 *Nucl. Fusion* **51** 094027

[19] Angioni C, Camenen Y, Casson F, Fable E, McDermott R, Peeters A and Rice J 2012 *Nucl. Fusion* **52** 114003

[20] Diamond P, Kosuga Y, Gürcan Ö, McDevitt C, Hahm T, Fedorczak N, Rice J, Wang W, Ku S, Kwon J *et al.* 2013 *Nucl. Fusion* **53** 104019

[21] Zonca F, Chen L and Santoro R A 1996 *Plasma Phys. Controlled Fusion* **38** 2011

[22] Zonca F, Chen L, Santoro R A and Dong J 1998 *Plasma Phys. Controlled Fusion* **40** 2009

[23] Zonca F and Chen L 2008 *Europhysics Lett.* **83** 35001

[24] Mett R and Mahajan S 1992 *Physics of Fluids B: Plasma Physics* **4** 2885–2893

[25] Berk H, Mett R and Lindberg D 1993 *Physics of Fluids B: Plasma Physics* **5** 3969–3996

[26] Lu Z X 2015 *Phys. Plasmas* **22** 052118

[27] Lu Z X, Fable E, Hornsby W, Angioni C, Bottino A, Lauber P and Zonca F 2017 *Phys. Plasmas* **24** 042502

[28] Liu Y, Lin Z, Zhang H and Zhang W 2017 *Nucl. Fusion* **57** 114001

[29] Briguglio S, Vlad G, Zonca F and Kar C 1995 *Phys. Plasmas* **2** 3711

[30] Briguglio S, Zonca F and Vlad G 1998 *Phys. Plasmas* **5** 3287

[31] Sauter O and Medvedev S Y 2013 *Computer Physics Communications* **184** 293

[32] Chavdarovski I and Zonca F 2009 *Plasma Phys. Controlled Fusion* **51** 115001

[33] Gorelenkov N, Van Zeeland M, Berk H, Crocker N, Darrow D, Fredrickson E, Fu G Y, Heidbrink W, Menard J and Nazikian R 2009 *Phys. Plasmas* **16** 056107

[34] Tsai S T and Chen L 1993 *Phys. Fluids B* **5** 3284

[35] Xie H, Li Y, Lu Z, Ou W and Li B 2017 *Phys. Plasmas* **24** 072106

[36] Lauber P, Günter S, Könies A and Pinches S D 2007 *J. Compu. Phys.* **226** 447

[37] Lauber P, Classen I, Curran D, Igochine V, Geiger B, Da Graca S, García-Muñoz M, Maraschek M, McCarthy P *et al.* 2012 *Nucl. Fusion* **52** 094007

[38] Wang X, Briguglio S, Chen L, Di Troia C, Fogaccia G, Vlad G and Zonca F 2011 *Phys. Plasmas* **18** 052504

[39] Zonca F and Chen L 2014 *Phys. Plasmas* **21** 072120

[40] Zonca F and Chen L 2014 *Phys. Plasmas* **21** 072121

[41] Zhang H S, Lin Z, Holod I, Wang X, Xiao Y and Zhang W L 2010 *Phys. Plasmas* **17** 112505

[42] Camenen Y, Idomura Y, Jolliet S and Peeters A 2011 *Nucl. Fusion* **51** 073039

[43] Lu Z X, Wang W, Diamond P, Tynan G, Ethier S, Chen J, Gao C and Rice J 2015 *Nucl. Fusion* **55** 093012

[44] Hornsby W, Angioni C, Lu Z X, Fable E, Erofeev I, McDermott R, Medvedeva A, Lebschy A, Peeters A G and the ASDEX Upgrade Team 2018 *Nucl. Fusion* **submitted**

[45] Pereverzev G 1998 *Phys. Plasmas* **5** 3529

[46] Kravtsov Y A, Forbes G and Asatryan A 1999 *Progress in optics* **39** 1–62

[47] Zhang W, Lin Z and Chen L 2008 *Phys. Rev. Lett.* **101** 095001